AIAA 97-0095
Global Wall Interference Correction and Control for the NWTC Transonic Test Section

W. L Sickles and F. W. Steinle Jr.
Sverdrup Technology, Inc., AEDC Group
Arnold Engineering Development Center
Arnold Air Force Base, Tennessee 37389

35th Aerospace Sciences Meeting and Exhibit
January 6-10, 1997 / Reno, NV

Global Wall Interference Correction and Control for the NWTC Transonic Test Section*

*W. L. Sickles** and F. W. Steinle Jr.†*
Sverdrup Technology, Inc., AEDC Group
Arnold Engineering Development Center
Arnold Air Force Base, TN 37389-6001

Abstract

As part of the currently postponed National Wind Tunnel Complex (NWTC) program, a computational fluid dynamic (CFD) study of a large transport configuration was performed using the AEDC chimera-overset grid XAIR Euler code. Wall porosity, porosity control for the reduction of wall interference, correction approach, and the impact of reference point selection on wall interference at transonic conditions (Mach Number 0.85) were studied. These effects were computationally investigated using a clean-wing model representative of the MD-11 aircraft which spanned 80 percent of the test section width. Global wall corrections were determined by a streamtube calculation of the interference flow field. Results of these computations showed that global corrections for Mach number at the 1/4 chord, 50-percent semi-span location with angle-of-attack correction based on matching wing lift gave very low interference. Investigation of control of porosity showed that very few zones were required to achieve superior results for global corrections and for model pressure distribution. Residual blockage gradient and flow-curvature effects are shown to be treatable by very small changes in side-wall divergence angle and model geometric changes that are equivalent to shearing the coordinate system aft of the wing-fuselage juncture.

Nomenclature

C_A	Axial-force coefficient
C_D	Drag coefficient
C_L	Lift coefficient
C_m	Pitching-moment coefficient
C_N	Normal-force coefficient
C_P	Pressure coefficient
M	Mach number
R	Wall resistance [Eq. (2)]
α	Angle of attack
ΔC_A	$C_{A\infty} - C_{AT}$
ΔC_D	$C_{D\infty} - C_{DT}$
ΔC_L	$C_{L\infty} - C_{LT}$
ΔC_m	$C_{m\infty} - C_{mT}$
ΔC_N	$C_{N\infty} - C_{NT}$
ΔC_P	$C_{P\infty} - C_{PT}$ [Eq. (1)]
θ	flow angle
τ	wall open area ratio, percent

Subscripts

T	tunnel condition
∞	free-air condition

1.0 Introduction

The facilities for the National Wind Tunnel Complex (NWTC) were being designed with the expectation that the maximum design Reynolds number would be achieved by testing models with spans up to 80 percent of the applicable test-section dimension. A consequence of the relatively large model-to-tunnel size ratio is that interference pro-

* The research reported herein was performed by the Arnold Engineering Development Center (AEDC), Air Force Materiel Command. Work and analysis for this research were performed by personnel of Sverdrup Technology, Inc., AEDC Group, technical services contractor for AEDC. Further reproduction is authorized to satisfy needs of the U. S. Government.

** Senior Member, AIAA.
† Associate Fellow, AIAA.

duced by the wind tunnel walls may be unacceptably large. The 80 percent span ratio is believed to be the largest value that can be tested with any reasonable chance of obtaining high-quality data. Data quality was of paramount importance for the NWTC; therefore, wall correction and wall control strategies were being investigated as an integral part of the development process. The preliminary criteria for wall interference at Mach number 0.85 were established for the uncorrected levels of blockage ($\Delta M \leq 0.003$), angle of attack ($\Delta\alpha \leq 0.15$ deg at $C_N = 1.0$), force coefficients ($\Delta C_N \leq 0.005$ and $\Delta C_A \leq 0.0003$), and pitching-moment coefficient corrections ($\Delta C_m \leq 0.01$). The intent of these criteria was to have the level of wall interference sufficiently low that reliable corrections could be made to the data to support meeting the overall uncertainty in the measurement of one drag count, ($C_D = 0.0001$). The purpose of the CFD evaluations of wall interference was to support validation of both the reasonableness of the interference and the development of the design features of the test section. The current paper summarizes the results obtained and documented in Ref. 1.

2.0 Computational Procedures

Wall interference estimates were based on Euler CFD flow-field solutions which were performed using the AEDC chimera-overset grid XAIR code.[2-4]

All computations were solved for flows about a generic representation of an MD-11 clean-wing configuration. All in-tunnel calculations were performed for a model that is scaled to span 80 percent of the tunnel width. The test-section geometry of this tunnel was 16 ft wide by 13 ft high with no corner fillets. The scaled model was 13.4 ft in length, and the model nose was positioned on centerline 16.3 ft downstream of the test-section entrance. The test section was 42 ft long. The scaled full-span configuration resulted in a solid blockage ratio of approximately 0.60 percent.

For all flow conditions under consideration, lateral symmetry was assumed about the center plane of the model. Therefore, only half of the flow field was modeled. Figure 1 shows a portion of the near-field grid system for the MD-11. The entire system contains nine grids with 1.1×10^6 grid points.

3.0 Wall Interference Procedure

In the current investigation, wall interference effects were predicted by two different methods, constant conditions and global corrections.

3.1 Method 1: Constant Conditions

In the constant conditions method, the wall interference effects are predicted at a constant geometric angle of attack and upstream Mach number by taking the difference between two CFD

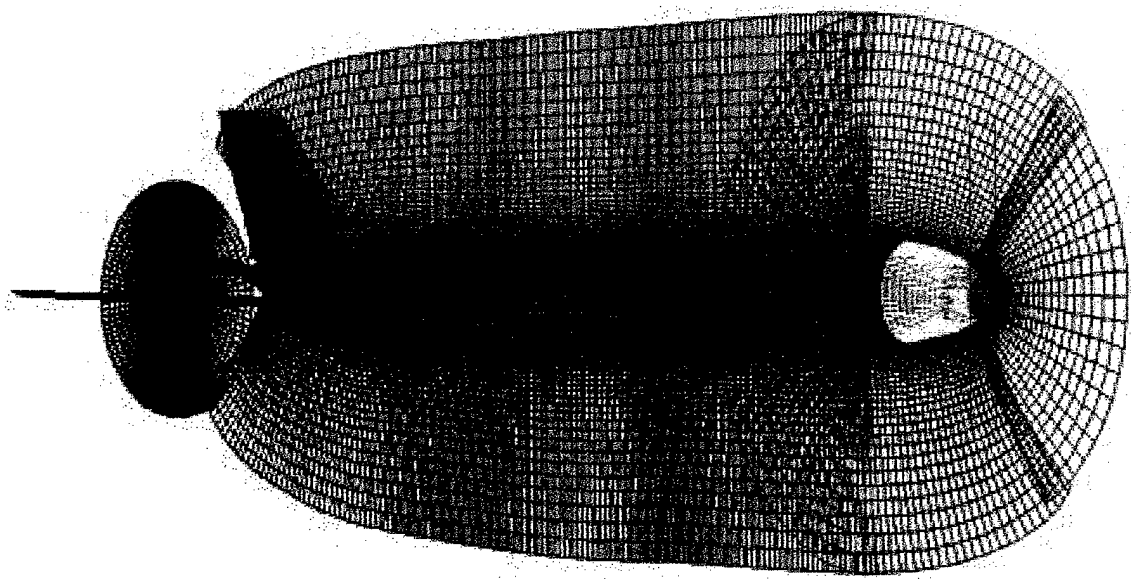

Fig. 1. Chimera inviscid grid system.

flow-field solutions. The first solution is a free-air flow-field calculation where the outer boundary of the computational domain extends well beyond the location of the tunnel walls. At the outer boundary of this domain, free-stream conditions are prescribed. The upstream and downstream outer boundaries are approximately four body lengths upstream and two body lengths downstream of the model, respectively. The vertical and horizontal planes of the outer boundary are approximately five tunnel heights from the centerline axis of the model. The second solution is an in-tunnel flow-field calculation at the same flow conditions where a wall boundary condition (Sec. 4.0) is prescribed at the tunnel walls. Here, the flow at the test section entrance is prescribed as uniform free-stream flow, while the flow at the test section exit is specified by an extrapolated boundary condition. A pair of flow-field solutions must be computed and compared to determine the wall interference at each selected flow condition. To minimize any possible difference due to grid resolution, meshes internal to the tunnel are identical. The local effects of wall interference on the model are examined by subtracting the calculated local pressure coefficient for the in-tunnel solution(C_{pT}) from the corresponding free-air solution($C_{p\infty}$) as

$$\Delta C_P = C_{P\infty} - C_{PT} \qquad (1)$$

and the global effects on forces and moments directly follow by pressure integration of the individual solutions and subtracting the result.

It is important to note that the wall interference procedure outlined above determines corrections to the model forces and moments at the fixed tunnel free-stream flow conditions and at a fixed geometric angle of attack. The result from this computation can be compared to the NWTC requirement for acceptable level of wall interference. Difference in viscous flow development obviously will affect the results. However, the method could include an integral boundary-layer technique to make a viscous correction

3.2 Method 2: Global Corrections

A more widely used wall interference procedure is to globally correct for blockage and flow-curvature effects of the tunnel walls by determining adjusted remote flow conditions. The objective of this procedure is to find equivalent free-air flow conditions that best match the tunnel data or, in this case, the in-tunnel calculations. The adjusted, equivalent conditions are typically determined by selecting a blockage correction (ΔM) and flow-angle correction ($\Delta\alpha$) to the free-air remote conditions which force the free-air and in-tunnel calculations to match at a given reference point (or points) on the model. In the present context, this procedure involves a minimum of two additional calculations.

The first additional flow-field calculation determines the adjustments to angle of attack and Mach number (ΔM and $\Delta\alpha$). This is done by performing an inverse computation of the interference flow field. The inverse computation involves a tunnel-empty flow-field or streamtube solution with the interference pressure distribution specified as the boundary condition at the tunnel boundaries. This interference pressure distribution is determined by subtracting the free-air pressure distribution from the tunnel pressure distribution, both of which are calculated at the tunnel walls from the aforementioned free-air and in-tunnel calculations. The resulting solution of the inverse flow field is interpolated onto the phantom model surface to provide disturbances (ΔM and $\Delta\alpha$) at selected reference points. A complete parametric analysis of the selection of the reference point location is beyond the scope of this investigation. Typically, the flow corrections are determined at a given spanwise location. At the given spanwise location, a different reference point is selected for determining ΔM and $\Delta\alpha$. The reference points are selected as the 1/4-chord location for ΔM and the 3/4-chord location for $\Delta\alpha$. The selection of these chordwise locations is based on classical theory.[5] The 3/4 chord for $\Delta\alpha$ is the classical point of choice to minimize pitching-moment residuals. Transonic flow features may require some other choice. Two spanwise locations, 25-percent and 50-percent semispan, were selected to investigate different correction strategies. Initial computations were performed using the corrections that were determined from both spanwise locations. As will be shown in the results, the 50-percent location yielded superior blockage corrections and was selected as the location of choice for the remaining computations.

The second additional flow-field calculation is performed to determine the free-air flow field at the adjusted remote conditions ($M + \Delta M$ and $\alpha + \Delta\alpha$). Using Eq. (1), the residual interference is determined by comparing the free-air flow-field calculation at adjusted conditions and the in-tunnel calculation at the original conditions (appropriately scaling load and pressure coefficients for the difference in dynamic pressure and adjusting stability-axis forces for differences in angle of attack).

The process to determine the optimum remote conditions is an iterative procedure where the inverse and free-air calculations are repeated until the residual interference is minimized. In the current investigations, only one inverse computation was required to obtain an accurate blockage or Mach number correction. Additional adjustments were made to the remote angle of attack to best match the wing lift between the in-tunnel and free-air calculations. This is similar to the technique used by Rizk.[6] The lift matching process typically took one additional free-air computation. However, because the interference on the model is spatially variant, residual wall interference still exists in the lift contribution from the other model components and in the other force and moment coefficients at these adjusted flow conditions. The residual is presumed to be significantly less than the total correction determined for the original, unadjusted flow conditions.

One advantage of this procedure is that differences in pressure gradient typically are much less than for Method 1. Hence, incremental corrections to account for viscous flow development differences are expected to be substantially smaller.

4.0 Wall Boundary Conditions

The porous slotted wall behavior was simulated by assuming and imposing a linear-homogeneous boundary condition representation at the test section walls. Provided that a slotted wall has sufficient slots, the local effect of the discrete slots rapidly diminishes, and the behavior of the wall is essentially uniform and continuous at a short distance from walls.[7] The NWTC slotted wall configuration was designed to have sufficient slots and to behave in this manner. Therefore, homogeneity was a reasonable assumption for this study. A boundary condition was selected that has been shown to be representative of the wall behavior in the NASA/ARC 11-ft Tunnel and was used for in-tunnel calculations. For this boundary condition, the cross-flow behavior at the wall is prescribed as

$$\frac{dC_P}{d\theta} = \frac{2}{\tau R} \tag{2}$$

where R is the wall resistance or porosity parameter, τ is wall porosity or wall open area ratio, and θ is the local flow angle at the wall. For all in-tunnel flow-field calculations, R = 19. To simulate test section walls with global uniform porosity, the value of τ was constant over all walls. To simulate variable porosity, τ was varied locally on all walls. This boundary condition was incorporated into the AEDC XAIR/chimera code and implemented by two methods. The first method calculates θ at each iteration in the flow-field solution, determines the wall pressure from Eq. (2), and then updates and imposes the internal energy as the boundary condition (along with extrapolated values of density and momentum). The second method calculates C_p, determines θ from the flow-field solution, and updates and specifies the appropriate component of momentum as the boundary condition. The second method was utilized when variable porosity was investigated, while the first method was used for all uniform porosity computations.

5.0 Results

The in-tunnel and free-air flow-field calculations about the model were performed on the AEDC Convex 3800. These inviscid computations typically required 12 CPU hours to converge. Steady-state convergence was considered met when all calculated model forces and moments coefficients remained unchanged to five significant digits.

5.1 Wall-Interference Computations at Constant Conditions (Method 1)

Baseline wall interference computations for several wall configurations and flow conditions were performed. This task involved making a number of in-tunnel flow-field calculations at different globally uniform, fixed values of wall porosity for transonic speed conditions and the corresponding

free-air flow-field calculations. The purpose of these calculations was to quantify the level of wall interference that can be expected for walls with globally uniform porosity. All calculations were performed, as well as the determination of wall interference increments, at the fixed transonic-speed conditions of $M_\infty = 0.85$, $\alpha = 0$ and 4 deg. In addition, in-tunnel computations were made at discrete porosities of $\tau = 4$, 6 , and 9 percent.

Table 1 shows the baseline computations, the flow conditions, and the resulting forces and moments wall interference increments using Method 1. The comparisons between the in-tunnel calculations and the corresponding free-air model pressure distributions for $\alpha = 4$ deg are shown in Figs. 2-4. The local pressure distributions show a significant longitudinal and spanwise variation in the increment between the free-air and in-tunnel calculations. The wing-pressure differences between the in-tunnel and free-air calculations appear to be minimized at 4 percent (Fig. 2). As the walls are opened for the transonic conditions, the effect on the model wing pressure distribution can be seen. The pressure level increases, the shock strength decreases, and the shock moves forward.

Table 1. Wall Interference Increments for Baseline Calculations (Constant Conditions Method)

M_∞	M_T	α_∞, deg	α_T, deg	τ, percent	ΔC_D	ΔC_L	ΔC_m
0.85	0.85	0	0	4	–0.0015	0.0017	0.0090
0.85	0.85	0	0	6	–0.0011	0.0107	–0.0010
0.85	0.85	0	0	9	–0.0007	0.0178	–0.0094
0.85	0.85	4	4	4	–0.0012	0.0021	0.0181
0.85	0.85	4	4	6	0.0012	0.0164	0.0041
0.85	0.85	4	4	9	0.0031	0.0286	–0.0091

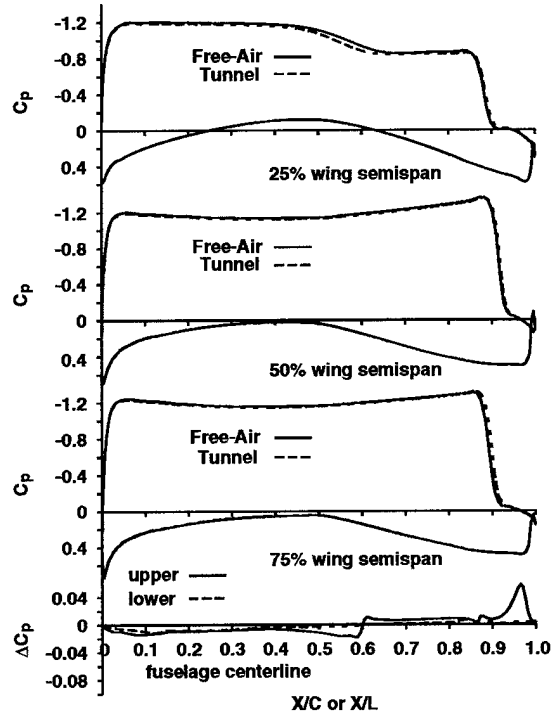

Fig. 2. Model pressures at fixed remote conditions, M = 0.85, $\alpha = 4$ deg, $\tau = 4$ percent, globally uniform.

Figure 5 summarizes the calculated wall interference force and moment increments for all the inviscid baseline calculations and shows the variation of those increments with porosity. The baseline calculations show that there is a significant variation in force and pitching-moment increments with uniform porosity and that wall interference varies significantly with model attitude. Because of the gradient of wall interference over the model, minimizing all forces and moments simultaneously cannot be accomplished with a uniform porosity. With uniform porosity and no corrections for blockage or

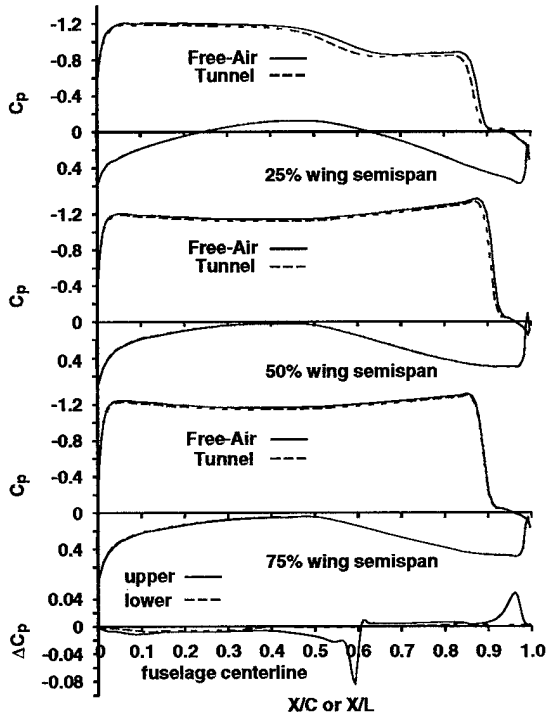

Fig. 3. Model pressures at fixed remote conditions, M = 0.85, $\alpha = 4$ deg, $\tau = 6$ percent, globally uniform.

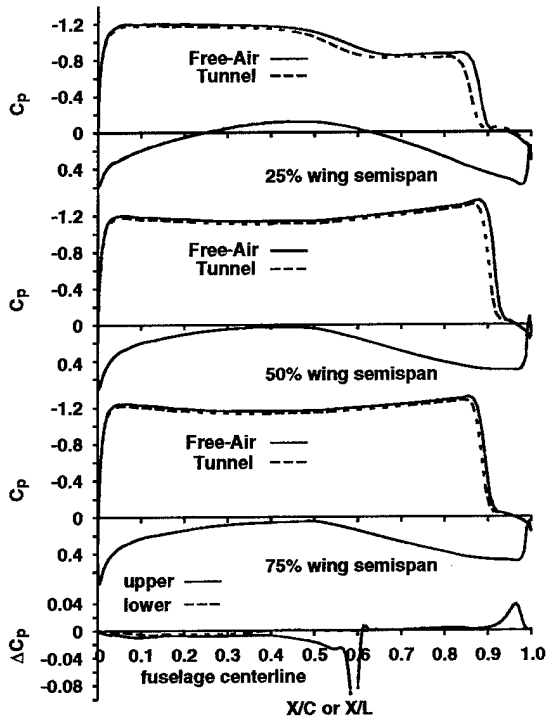

Fig. 4. Model pressures at fixed remote conditions, M = 0.85, α = 4 deg, τ = 9 percent, globally uniform.

flow curvature, the interference increments do not meet the NWTC wall interference criteria for transonic flow conditions.

Controllable walls were considered as a method to meet the stringent NWTC data quality specifications. As seen in the baseline computations, uniform porosity does not provide the desired data quality for transonic flows. Variable porosity was investigated to show the possible benefits of controllable walls in meeting these data quality specifications. Two variable-porosity methods were computationally investigated using the linear-homogeneous boundary conditions. In the first method, it was assumed that there is an infinite number of control segments over the walls. With this method, the porosity varies locally over the test section walls to best match the local wall behavior determined from the free-air computation. This method will be referred to as distributed porosity control and represents the absolute best that can be done with variable porosity alone. In the second method, limited control was imposed. The wall was segmented, and the porosity was fixed laterally or vertically over the patch and allowed to vary linearly in the longitudinal direction. The longitudinal variation was constrained to be piecewise continu-

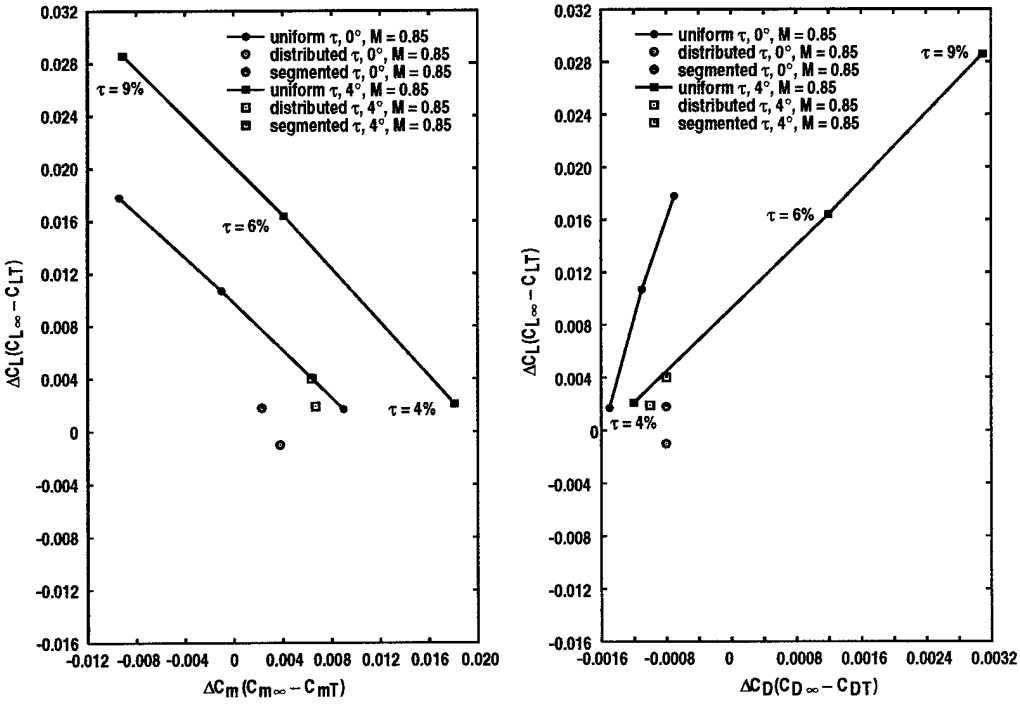

Fig. 5. Wall interference increments at fixed remote conditions.

ous between patches. This method will be referred to as segmented porosity control and represents a more realistic implementation of variable wall control. Both of these were utilized to investigate variable porosity for the two transonic flow cases.

From the free-air baseline calculations, ideal values of the local porosity for the transonic cases were determined. This was accomplished by interpolating the free-air flow field onto a surface equivalent to the tunnel boundary and then calculating the local pressure and flow angle distributions to determine the ideal local cross-flow properties. Using Eq. (2), the local values of porosity were determined. Practical considerations (e.g., the porosity cannot be negative) made it necessary to constrain the porosity such that $10\% \geq \tau \geq 0\%$ (solid wall). This distribution of porosity was imposed as the boundary conditions and the in-tunnel flow-field solutions were calculated. The results of these calculations were compared to the corresponding free-air solutions. The force increments are shown in Table 2. The wall interference is significantly reduced over the uniform porosity baseline cases, as can be seen in Fig. 5. The model pressure comparisons for α = 4 deg are shown in Fig. 6. The results from these calculations show a significant reduction in wall interference by incorporating variable porosity control. Figure 7 shows the corresponding wall cross-flow distribution (flow angle vs. pressure). The wall cross-flow distribution for the distributed porosity cases and the free air shows good agreement except for a slight overshoot in pressure coefficient at the model center. This overshoot is caused by an acceleration of the flow from the upstream solid wall patch. The results of the distributed porosity computations show a significant benefit to utilizing variable porosity.

A segmented controllable wall was investigated by developing a patchwork of controllable seg-

Table 2. Wall Interference Increments for Variable Porosity Calculations (Constant Corrections Method)

M_∞	M_T	α_∞, deg	α_T, deg	τ, percent	ΔC_D	ΔC_L	ΔC_m
0.85	0.85	0	0	dist	–0.0008	–0.0010	0.0038
0.85	0.85	0	0	seg	–0.0008	0.0018	0.0023
0.85	0.85	4	4	dist	–0.0010	0.0019	0.0067
0.85	0.85	4	4	seg	–0.0008	0.0040	0.0064

dist = distributed porosity variation
seg = segmented porosity variation

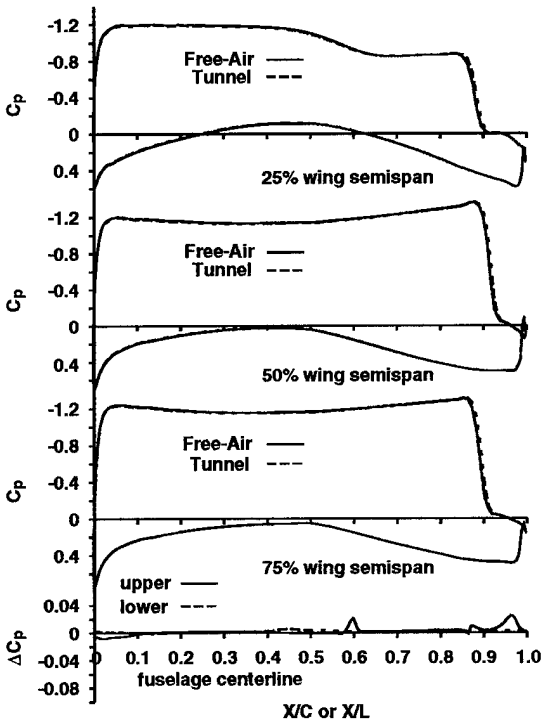

Fig. 6. Model pressures at fixed remote conditions, M = 0.85, α = 4 deg, distributed porosity.

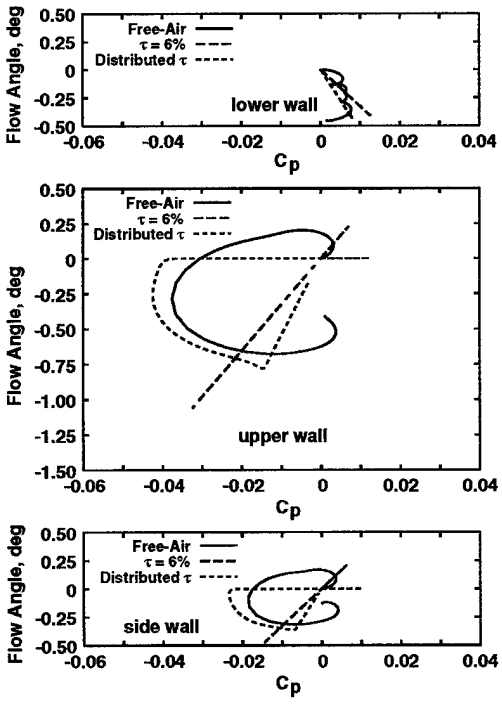

Fig. 7. Wall signature comparison at M = 0.85, α = 4 deg, distributed porosity.

ments. The goal was to simulate a wall where the flow through the slots is throttled by using movable, plenum-side cut-off plates. The cut-off plates would allow the porosity to be linearly varied in the flow direction. In addition, the goal was to develop a segmented wall that could be feasibly implemented. The patchwork was developed by examining the wall distributions and deciding where the most and least wall control is needed. The most control is needed in regions of highest gradients, e.g., model wing, while the least control is in the regions of minimum gradients, e.g., upstream and downstream. Figure 8 shows the patchwork used for the computations. This configuration shows six streamwise-controllable sections on the top and side walls and one on the bottom wall. Implementation of this configuration would require six controllable segments along all or selected slots on the top and side walls and one control segment for all or selected bottom wall slots.

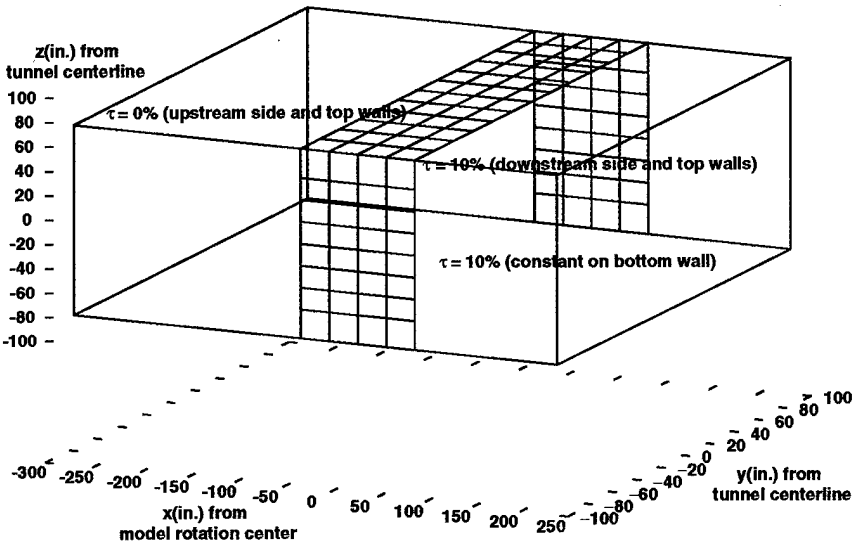

Fig. 8. Porosity segmentation for segmented porosity runs.

The longitudinal porosity variation was determined by anchoring the porosity at the upstream and downstream ends to be equal to the interpolated free-air porosity and linearly interpolating over the length of the segment. This constrains the distribution to be piecewise continuous between segments. The wall interference results of these calculations are also shown in Table 2 as well as in Fig 5. The wall interference increments are comparable to the ideal distributed porosity results. The model pressure comparison in Fig. 9 and corresponding wall signature in Fig. 10 are almost identical to the distributed porosity results. These results show that limited segmented control can reduce wall interference as well as infinite control, provided the segmentation is strategically placed. Additional work would be required to determine the optimum placement and minimum number of control segments, the solution to the pressure overshoot in the wall signature, and an active wall control strategy.

5.2 Wall Interference Computations with Global Corrections (Method 2)

For selected uniform and segmented porosity calculations, adjustments to free-air flow-field angle of attack and Mach number were determined to find equivalent free-air conditions that best match the

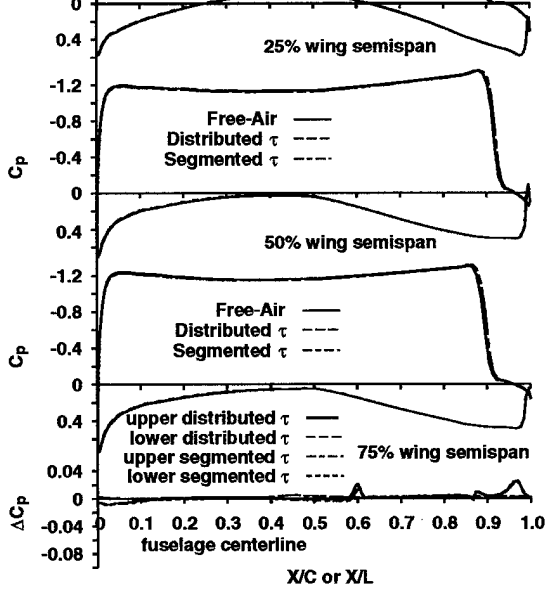

Fig. 9. Model pressures at fixed remote conditions, M = 0.85, α = 4 deg, segmented porosity.

in-tunnel calculations. The purpose of these computations was to determine the residual interference after the computations have been corrected for first-order blockage and flow-curvature effects. The flow-field adjustments were determined using the procedure described in Sec. 3.0. Five cases were selected and are shown in Table 3. These cases include two porosity distributions at $\alpha = 0$ deg (a uniform porosity, τ = 6 percent, and the segmented porosity distribution) and three porosity distributions at $\alpha = 4$ deg (two uniform porosities, $\tau = 4$ and 6 percent, and the segmented distribution porosity).

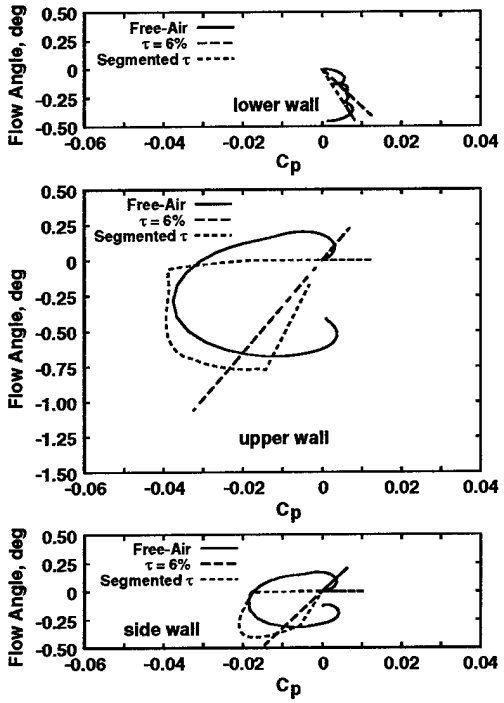

Fig. 10. Wall signature comparison at M = 0.85, $\alpha = 4$ deg, segmented porosity.

Figure 11 shows representative streamtube results for the M = 0.85, $\alpha = 4$ deg, and $\tau = 6$ percent case interpolated onto a phantom surface of the MD-11 wind/body/horizontal tail configuration. Shown are the Mach number and flow curvature effects of the walls. The contour plots show a significant spanwise and longitudinal gradient in the

Table 3. Wall Interference Increments at Adjusted Free-Stream Conditions (Global Corrections Method)

M_∞	M_T	α_∞, deg	α_T, deg	τ, percent	ΔC_D	ΔC_L	ΔC_m	Ref. Loc., percent
0.84800	0.85	-0.1000	0	6	–0.0011	0.0108	–0.0011	25
0.84900	0.85	-0.1000	0	6	–0.0010	–0.0023	0.0084	50
0.85048	0.85	-0.0294	0	seg	–0.0007	–0.0006	0.0036	50
0.84700	0.85	3.8300	4	6	–0.0027	–0.0103	0.0235	25
0.84850	0.85	3.8400	4	6	–0.0014	–0.0041	0.0177	50
0.84940	0.85	3.9182	4	4	–0.0023	–0.0075	0.0243	50
0.85096	0.85	3.9320	4	seg	–0.0006	0.0004	0.0074	50

Tunnel forces and moments adjusted to the dynamic pressure and angle of attack of the free-air conditions.
seg = segmented porosity variation

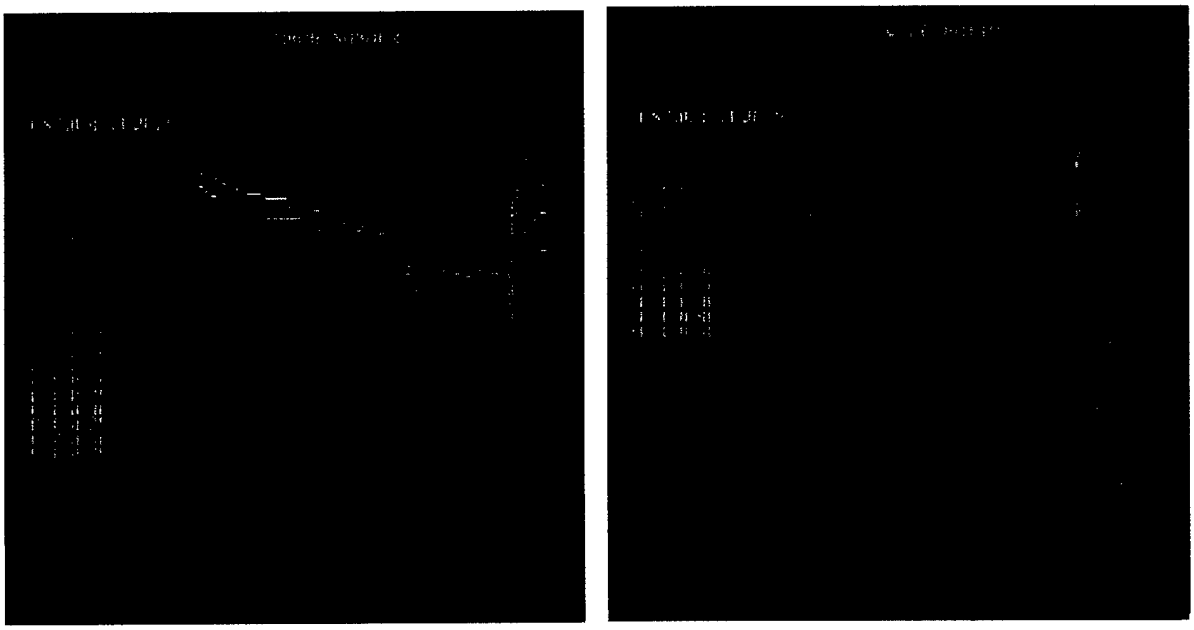

a. Blockage b. Flow angle (radians)

Fig. 11. Interference flow-field solution.

interference field. The streamtube results were used to determine the adjustments to the remote conditions.

Initially, remote condition corrections were determined from two spanwise reference locations in the streamtube calculations. These spanwise locations were the 25- and 50-percent semispan locations. Figures 12 and 13 show the model pressure agreement for these initial calculations, while Table 3 shows the residual force and moment differences at the corrected conditions. The calculated in-tunnel pressures and loads were all corrected to the free-air dynamic pressure and angle of attack. A significant improvement in the wing pressure comparison can be seen, particularly for the flow determined at the 50-percent semispan location (compare Fig. 13 to Fig. 3). The pressure comparisons clearly show the advantage of using the 50-percent semispan location as the reference point. Similar improvements in the wing pressure agreement were observed for the other fixed porosity cases. For the remaining cases, the corrections to the remote conditions were determined at the 50-percent semispan reference.

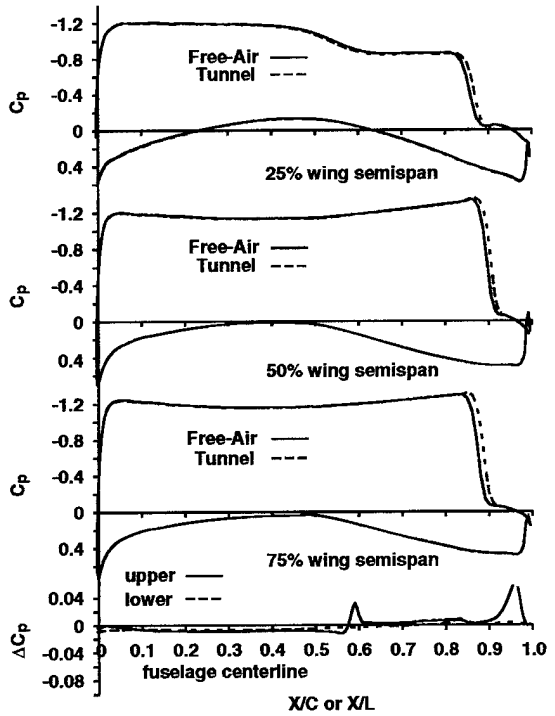

Fig. 12. Model pressures at adjusted remote conditions, M = 0.847, α = 3.83 deg, τ = 6 percent, globally uniform, reference points located at 25 percent semispan.

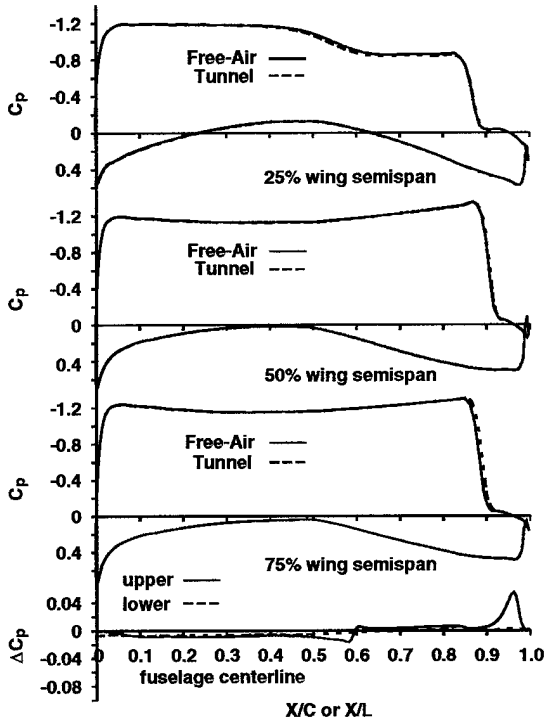

Fig. 13. Model pressures at adjusted remote conditions, M = 0.8485, α = 3.84 deg, τ = 6 percent, globally uniform, reference points located at 50 percent semispan.

Model pressure comparisons for the segmented porosity are shown in Fig. 14. Pressure agreement for the segmented porosity was already quite good and only a small improvement is noticed.

Although a significant improvement was made in the wing pressure agreement, pressure differences still exist on the aft fuselage. The differences are primarily due to the longitudinal gradients in flow curvature and velocity between the wing and the tail. These gradients can be seen in the inverse computations of Fig. 11.

This case yielded a difference in flow angle of 0.172 deg between the wing and tail reference points. Normally, the difference in flow angle is resolved by modifying the tail angle. A different approach was used here. The whole aft fuselage was warped aft of the wing root. Each longitudinal grid plane downstream of the wing root was rotated

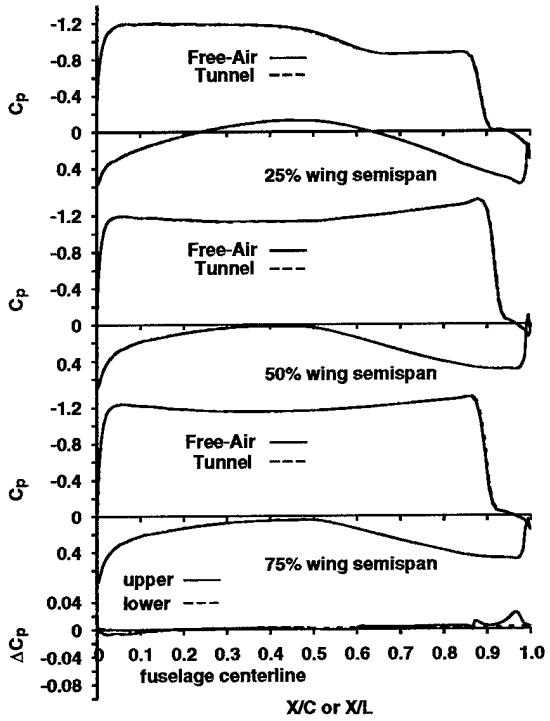

Fig. 14. Model pressures at adjusted remote conditions, M = 0.85096, α = 3.932 deg, segmented τ, globally uniform, reference points located at 50 percent semispan.

about a wing root reference. The rotation angle was determined by a linearly weighted flow angle distribution based on the distance from the wing root. Figure 15 shows the model pressure comparisons for the warped fuselage calculations. Significant improvement was obtained in the aft fuselage agreement (see Fig. 13 for comparison). An improvement was also seen in the load increments shown in Table 4. The process of warping the fuselage is similar to the shearing techniques used to account for aeroelastic distortion.

The longitudinal velocity gradient or tunnel buoyancy is normally eliminated by adjusting the wall angle. Side wall divergence was numerically attempted. However, problems with coupling the side wall divergence angle and the porous wall boundary condition were not successfully resolved before the completion of the project. The correction approach to Mach number gradient by controlling the side wall angle is practical and one-dimensional flow analysis revealed only a small change to wall angles of less than 0.03 deg is needed.

Force and moment increments at the given conditions are compared to those at the adjusted conditions in Fig. 16. The load increments changed significantly for the adjusted remote conditions. For all cases except $\alpha = 4$ deg, $\tau = 4$ percent and $\alpha = 0$ deg, $\tau = 6$ percent (remained unchanged), the magnitude of the lift increment decreased, and for all cases except α = 0 deg, τ = 6 percent, the magnitude of the pitching-moment increments increased. The increasing pitching moment increments show the need to include tail incidence corrections as part of the correction strategy. With a combination of using

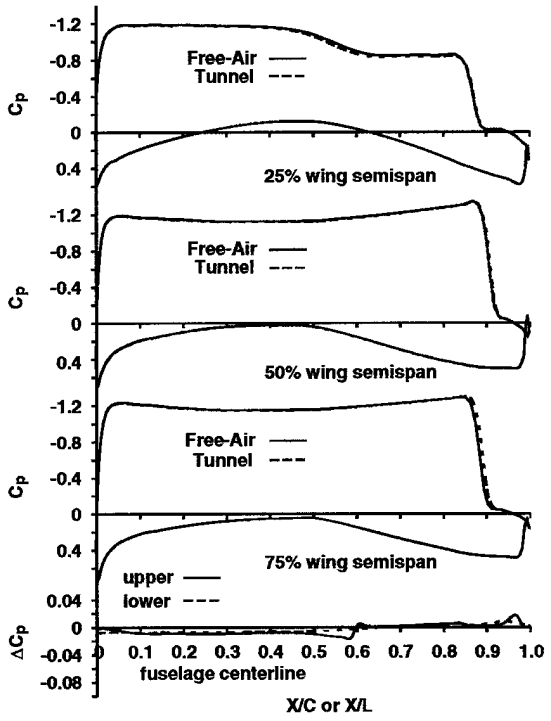

Fig. 15. Model pressures at adjusted remote conditions, M = 0.8485, α = 3.84 deg, τ = 6 percent, globally uniform, reference points located at 50 percent semispan, warped fuselage.

Table 4. Wall Interference Increments for Warped Aft Fuselage and Baseline Configurations (Global Corrections Method)

M_∞	M_T	α_∞, deg	α_T, deg	τ, percent	ΔC_D	ΔC_L	ΔC_m	Remarks
0.8485	0.85	3.84	4	6	–0.0014	–0.0041	0.0177	BC
0.8485	0.85	3.84	4	6	–0.0007	–0.0022	–0.0025	WF

Tunnel forces and moments adjusted to the dynamic pressure and angle of attack of the free-air conditions.
BC = baseline configuration
WF = warped fuselage

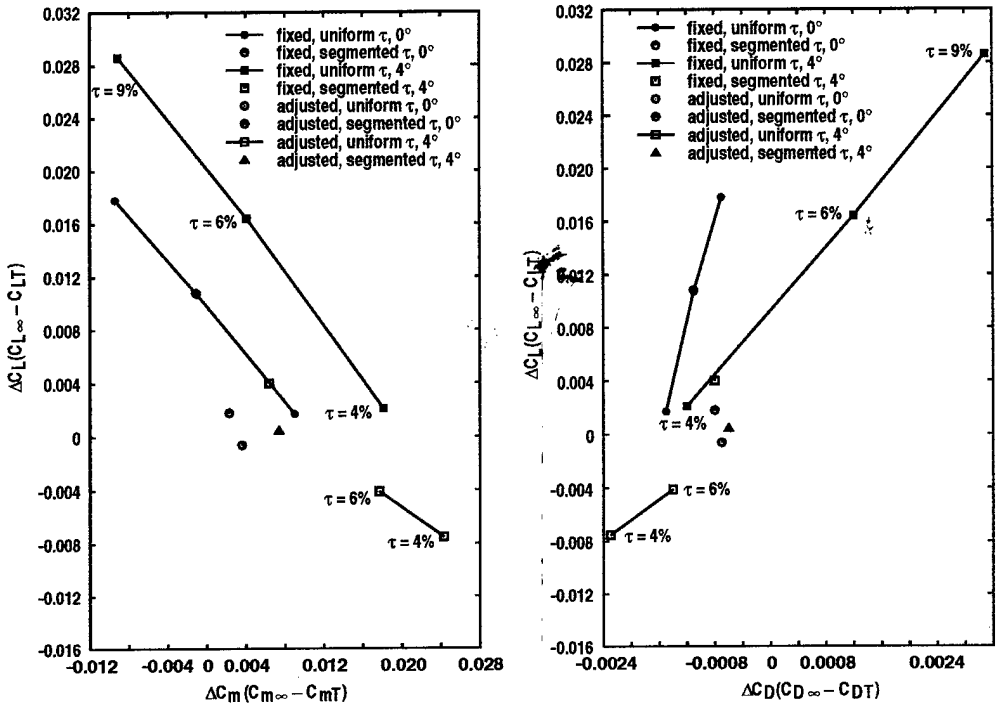

Fig. 16. NWTC wall interference comparison, fixed vs. adjusted conditions, nominal M = 0.285.

Table 5. Wall Interference Increments for $\Delta C_{L(wing)}$ Minimized (Global Corrections Method)

M_∞	M_T	α_∞, deg	α_T, deg	τ, percent	ΔC_D	ΔC_L	ΔC_m	Ref. Loc., percent
0.84800	0.85	–0.0770	0	6	–0.0012	0.0084	–0.0085	25
0.84900	0.85	–0.0960	0	6	–0.0011	–0.0018	0.0081	50
0.85048	0.85	–0.0326	0	seg	–0.0007	–0.0009	0.0039	50
0.84700	0.85	3.8960	4	6	–0.0021	–0.0037	0.0195	25
0.84850	0.85	3.8389	4	6	–0.0014	–0.0043	0.0178	50
0.84940	0.85	3.9452	4	4	–0.0021	–0.0053	0.0229	50
0.85096	0.85	3.9054	4	seg	–0.0008	–0.0021	0.0089	50

Tunnel forces and moments adjusted to the dynamic pressure and angle of attack of the free-air conditons.
seg - segmented porosity variation

variable porosity, side wall divergence control, and adequate wall corrections, it does appear that the flow quality specifications for the NWTC can be met.

Loads were calculated for each model component. Forces and moments contribution for the wing, body, horizontal tail, and vertical tail were tabulated for each run. With this tabulation, adjustments to angle of attack were determined to minimize the wing lift difference. The lift difference between the in-tunnel and free-air solution was driven to less than one count in lift coefficient (0.0001). Once the wing lift slope was determined for each nominal angle of attack, the process required only one additional calculation. The purpose of these computations was to explore additional fine tuning of the above correction strategy. This minimization process was performed for the cases in Table 3 (as well as others). Figures 17 and 18 show the model pressures comparison. The residual interference loads increments are shown in Table 5. Comparison of the force and moment increments at the given conditions to those at the adjusted conditions with minimized wing lift increments is shown in Fig. 19. No significant differences are seen in the total force and moment increments between these results and the results presented in Fig. 16. Table 6 shows the wing force and moment increments before and after the minimization process. Note that the wing lift is matched.

6.0 Conclusions

A computational investigation of wall interference in the 13 × 16-ft NWTC test section was performed for transonic conditions. The study involved

Table 6. Force and Pitching-Moment Increments Before and After Wing-Lift Minimization (Global Corrections Method)

Conditions			Before Minimization					After Minimization					Ref. Loc., percent
M_∞	M_T	τ, percent	α_∞, deg	α_T, deg	ΔC_D	ΔC_m	ΔC_L	α_∞, deg	α_T, deg	ΔC_D	ΔC_m	ΔC_L	
0.84800	0.85	6	–0.1000	0	–0.0005	0.0034	–0.0022	–0.0770	0	–0.0005	0.0020	0	25
0.84900	0.85	6	–0.1000	0	–0.0003	0.0017	–0.0004	–0.0960	0	–0.0004	0.0014	0	50
0.85048	0.85	seg	---	0	–0.0001	0.0006	0.0003	–0.0326	0	–0.0001	0.0008	0	50
0.84700	0.85	6	3.8300	4	–0.0014	0.0089	–0.0058	3.8960	4	–0.0009	0.0042	0	25
0.84850	0.85	6	3.8400	4	–0.0002	0.0020	0.0001	3.8389	4	0.0001	0.0021	0	50
0.84940	0.85	4	3.9182	4	0.0009	0.0052	–0.0019	3.9452	4	–0.0007	0.0039	0.0001	50
0.85096	0.85	seg	3.9320	4	0.0000	–0.0001	0.0022	3.9054	4	–0.0002	0.0013	0	50

Tunnel forces and moments adjusted to the dynamic pressure and angle of attack of the free-air conditions
seg = segmented porosity variation

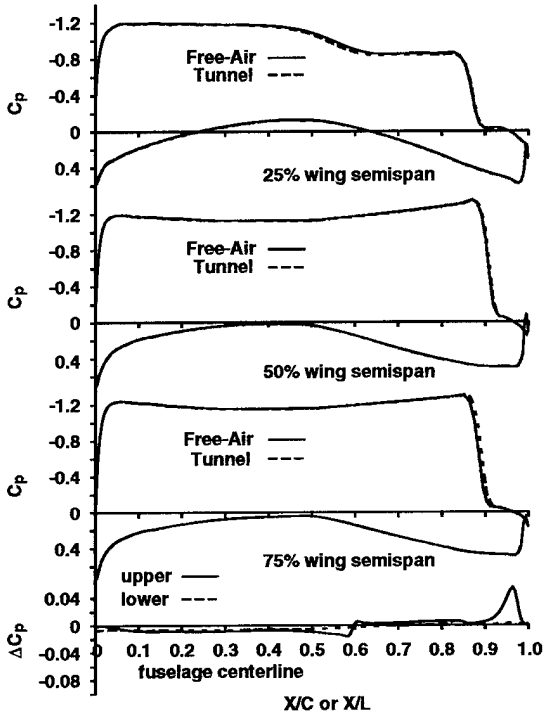

Fig. 17. Model pressures at adjusted remote conditions, M = 0.8485, α = 3.8389 deg, τ = 6 percent, globally uniform, ΔC_L (wing) minimization for 3.84 deg case.

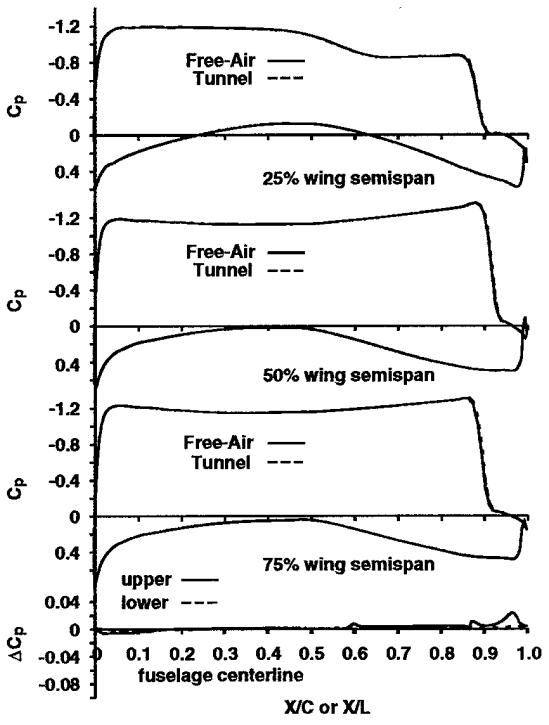

Fig. 18. Model pressures at adjusted remote conditions, M = 0.85096, α = 3.9054 deg, segment porosity, globally uniform, ΔC_L (wing) minimization for 3.932 deg case.

computing the flow over a clean-wing MD-11 type model that spanned 80 percent of the tunnel width. Steady-state converged solutions to the Euler equations were obtained using the AEDC XAIR code. A linear homogeneous wall boundary condition was used that is representative of the slotted walls in the NASA/ARC 11-ft tunnel. The investigation involved computing a number of baseline calculations to determine the variation of wall interference with porosity at fixed geometric angle of attack and Mach number. The benefit of using controllable walls was investigated. Wall correction strategies were also investigated.

The baseline calculations showed that there is a significant variation in force and pitching-moment increments with uniform porosity and that wall interference varies significantly with model attitude. Because of the gradient of wall interference over the model, minimizing all forces and moments

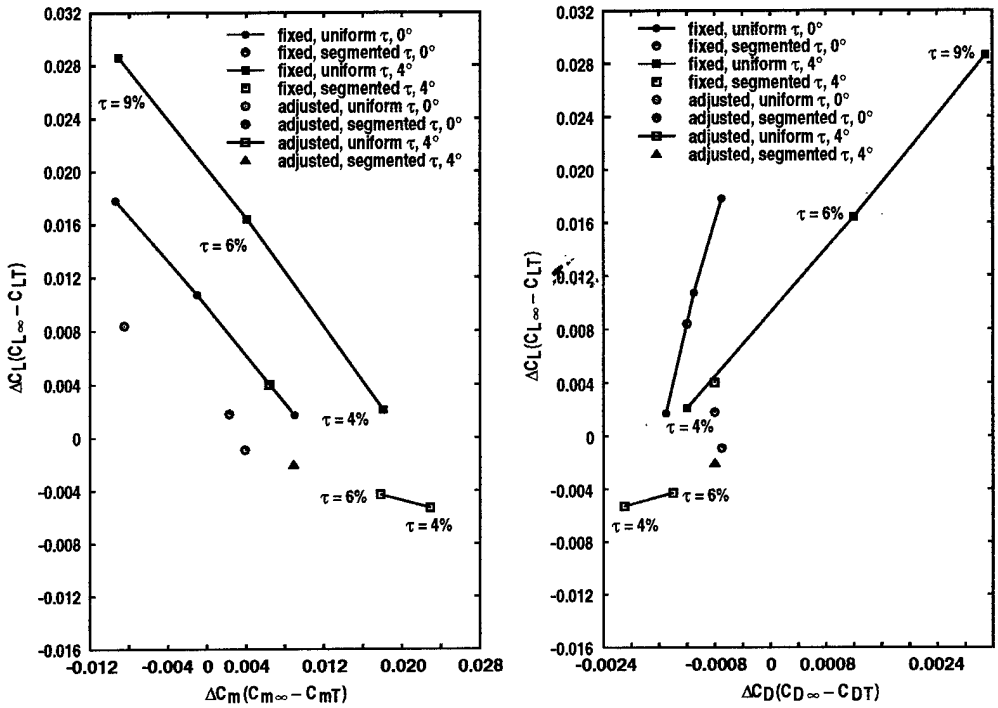

Fig. 18. NWTC wall interference comparison, fixed vs. adjusted, minimized ΔC_L (wing), nominal M = 0.85.

simultaneously cannot be accomplished with a uniform porosity. With uniform porosity and no corrections for blockage or flow curvature, the interference increments did not meet the wall interference criteria for transonic flow conditions.

Variable porosity schedules based on the free-air solutions were determined at two transonic flow conditions. Two schedule types were used, one with an infinite number of control segments and another with finite control segments. The results showed that variable porosity significantly reduced the wall interference. The benefit and even the necessity of using controllable walls to meet data quality specifications was clearly shown. Ideal distribution of porosity with infinite number of control segments yielded comparable results with limited finite segmented control. Additional work is required to determine the optimum placement and minimum number of control segments, the solution to the pressure overshoot in the wall signatures, and an on-line, feed-forward wall control strategy to predict wall settings. The current investigation did show that, with a limited number of control segments, wall interference can be greatly reduced.

Free-air calculations were performed at adjusted remote conditions for several cases to examine wall correction strategies and to determine residual interference after first-order Mach number and flow curvature effects were considered. Adjusted conditions were determined at given reference points from an inverse computation of the interference field. Corrections determined at two different spanwise locations showed that the 50-percent semispan location yielded superior blockage corrections. Wing pressure comparisons at the adjusted conditions showed a significant improvement over the pressure comparisons at the given conditions. For most cases, the magnitude of the lift increment decreased, but the magnitude of the pitching-moment increments increased. The increasing pitching-moment increments showed the need to include tail incidence corrections as part of the correction strategy. The tail incidence was effectively changed by warping the aft fuselage to account for flow curvature gradients between the wing and the tail. Significant improvement was obtained in the aft fuselage pressure agreement and the pitching-moment increments. Investigating side wall control to eliminate tunnel buoyancy was not completed

and should be performed to confirm the one-dimensional analysis.

With a combination of using controllable porosity, possible side-wall angle, and adequate wall corrections, the results indicated that the transonic wall interference specifications for the NWTC can be met, and the resulting level of wall corrections needed is small.

7.0 Acknowledgements

The authors would like to acknowledge the efforts of Dr. R. H. Nichols and Mr. C. T. Bangasser for the development of the grid systems for the MD-11 and Mr. A. G. Denny and Mr. C. T. Bangasser for their assistance in running the inviscid solutions.

8.0 References

1. Sickles, W. L. and Steinle, F. W., Jr., "NWTC Slotted Wall Design Effort: Computational Task," National Wind Tunnel Complex Project Archive, CDROM Vol. 1, Document No. 648, May 1996.

2. Benek, J. A., Steger, J. L., Dougherty, F. C., and Buning, P. G. "Chimera: A Grid-Embedding Technique," AEDC-TR-85-64 (AD-A167466), April 1986.

3. Suhs, N. E. and Tramel, R. W. "PEGSUS 4.0 User's Manual," AEDC-TR-91-8 (AD-A280608), October 1991.

4. Beam, R. and Warming, R. F. "An Implicit Finite-Difference Algorithm for Hypersonic Systems In Conservative Form," *Journal of Computational Physics*, Vol. 22, September 1976, pp. 87-110.

5. Garner, H. C., Rogers, E. W. E., Acum, W. E. A., and Maskell, E. E. "Subsonic Wind Tunnel Wall Corrections," *AGARDograph* 109, October 1966.

6. Rizk, M. H. "Improvements in Code TUNCOR for Calculating Wall Interference Corrections in the Transonic Regime," AEDC-TR-86-6 (AD-A166766), March 1986.

7. Crites, R. C. and Steinle, F. W., Jr. AIAA Paper No. 95-0107, presented at the AIAA 31st Aerospace Sciences Meeting, Reno, NV, January 1995.

REPORT DOCUMENTATION PAGE

Form Approved
OMB No. 0704-0188

1. AGENCY USE ONLY *(Leave blank)*	2. REPORT DATE	3. REPORT TYPE AND DATES COVERED
	January 1997	Technical Society Paper

4. TITLE AND SUBTITLE
Global Wall Interference Correction and Control for the National Wind Tunnel Complex Transonic Test Section
AIAA Paper No. 97-0095

5. FUNDING NUMBERS

6. AUTHOR(S)
W. L. Sickles and F. W. Steinle, Jr.

7. PERFORMING ORGANIZATION NAME(S) AND ADDRESS(ES)
Sverdrup Technology, Inc./AEDC Group
740 Fourth Street
Arnold Air Force Base, Tennessee 37389-6001

8. PERFORMING ORGANIZATION REPORT NUMBER

9. SPONSORING/MONITORING AGENCY NAME(S) AND ADDRESS(ES)
Arnold Engineering Development Center
Arnold Air Force Base, TN 37389

10. SPONSORING/MONITORING AGENCY REPORT NUMBER

11. SUPPLEMENTARY NOTES
35th AIAA Aerospace Sciences Meeting, Reno, NV, January 6-9, 1997,

12a. DISTRIBUTION AVAILABILITY STATEMENT
Approved for public release; distribution unlimited.

12b. DISTRIBUTION CODE
A

13. ABSTRACT *(Maximum 200 words)*
As part of the currently postponed National Wind Tunnel Complex (NWTC) program, a computational fluid dynamic (CFD) study of a large transport configuration was performed using the AEDC chimera-overset grid XAIR Euler code. Wall porosity, porosity control for the reduction of wall interference, correction approach, and the impact of reference point selection on wall interference at transonic conditions (Mach Number 0.85) were studied. These effects were computationally investigated using a clean wing model representative of the MD-11 aircraft which spanned 80 percent of the test section width. Global wall corrections were deter-mined by a streamtube calculation of the interfer-ence flow field. Results of these computations showed that global corrections for Mach number at the 1/4 chord, 50-percent semi-span location with angle-of-attack correction based on matching wing lift gave very low interference. Investigation of con-trol of porosity showed that very few zones were required to achieve superior results for global corrections and for model pressure distribution. Residual blockage gradient and flow-curvature effects are shown to be treatable by very small changes in side-wall divergence angle and model geometric changes that are equivalent to shearing the coordinate system aft of the wing-fuselage juncture.

14. SUBJECT TERMS
Wall interference corrections, porous walls, tunnel flow quality, National Wind Tunnel Complex, NWTC, slotted walls, ventilated walls

15. NUMBER OF PAGES
16

16. PRICE CODE

17. SECURITY CLASSIFICATION OF REPORT	18. SECURITY CLASSIFICATION OF THIS PAGE	19. SECURITY CLASSIFICATION OF ABSTRACT	20. LIMITATION OF ABSTRACT
Unclassified	Unclassified	Unclassified	UL